Three-Dimensional Fault Structure Inferred from a Refined Aftershock Catalog for the 2015 Gorkha Earthquake, Nepal

Masumi Yamada,[1] Thakur Kandel,[2] Koji Tamaribuchi[3] Abhijit Ghosh[4]

Abstract.
In this paper, we created a well-resolved aftershock catalog for the 2015 Gorkha earthquake in Nepal by processing 11 months of continuous data using an automatic onset and hypocenter determination procedure. Aftershocks were detected by the NAMASTE temporary seismic network that is densely distributed covering the rupture area and became fully operational about 50 days after the mainshock. The catalog was refined using a joint hypocenter determination technique, and an optimal one-dimensional (1D) velocity model with station correction factors determined simultaneously. We found around 15,000 aftershocks with the magnitude of completeness of M2. Our catalog shows that there are two large aftershock clusters along the north side of the Gorkha–Pokhara anticlinorium and smaller shallow aftershock clusters in the south. The patterns of aftershock distribution in the northern and southern clusters reflect the complex geometry of the Main Himalayan Thrust. The aftershocks are located both on the slip surface and through the entire hanging wall. The 1D velocity structure obtained from this study is almost constant at a P-wave velocity (Vp) of 6.0 km/s for a depth of 0–20 km, similar to Vp of the shallow continental crust.

Introduction

On April 25, 2015, an earthquake (Mw 7.8) in central Nepal (later referred to as the Gorkha earthquake) caused significant damage, including 8979 fatalities. This was the largest earthquake that occurred after the installation of the national seismic network in Nepal. The earthquake ruptured the Main Himalayan Thrust (MHT), the plate boundary between India and the Tibetan Plateau [Galetzka et al., 2015; Avouac et al., 2015].

The aftershock activity was studied immediately after the earthquake. Adhikari et al. [2015] manually processed the seismic data of the permanent national seismic network in Nepal and presented a temporal and spatial distribution of the early aftershocks. Baillard et al. [2017] processed the same data with automatic onset and hypocenter determination procedures and created an aftershock catalog for the three months following the earthquake. Bai et al. [2016] used a seismic array near the China–Nepal border and located early aftershocks using the double-difference earthquake relocation technique. Aftershock activities were also studied using global seismic data [e.g. Letort et al., 2016; Wang et al., 2017]

Although the horizontal distribution is roughly consistent among these studies, the hypocenter depths exhibit a larger uncertainty, making it difficult to clarify the relationship between the aftershocks and the fault structure. The mainshock rupture surface is located on the MHT décollement based on the hypocenter depth and moment tensor mechanism [Adhikari et al., 2015; McNamara et al., 2017; Baillard et al., 2017]. However, the aftershocks may be shallower [Bai et al., 2016; Baillard et al., 2017], deeper [McNamara et al., 2017], or on the boundary [Letort et al., 2016; Wang et al., 2017] of the MHT shear zone. Aftershocks identified using far-field data are strongly influenced by the velocity structure, and the data are limited to large earthquakes. Variations in the local subsurface structure also result in estimation errors.

Another uncertainty is the three-dimensional (3D) structure of the MHT. Nepal lies on the collision zone between the Indian Plate and the Eurasian Plate, and the Indian lithosphere underthrusts beneath the Himalayas along the MHT. Three major north-dipping faults formed because of this collision—the Main Frontal Thrust (MFT), the Main Boundary Thrust (MBT), and the Main Central Fault (MCT)—from the south to the north. Figure 1 shows the geological map of Nepal modified after Dahal [2006]. The north–south (NS) section, in the direction of motion of the Indian Plate, has been thoroughly studied using microseismicity [e.g. Pandey et al., 1995, 1999] and geophysical tools such as receiver function [e.g. Tilmann et al., 2003; Nábelek et al., 2009]. Although it is believed that the variation in the east–west (EW) direction is largely homogeneous, the structure is not well studied.

In order to improve the 3D spatial resolution of the aftershock activity, we used the temporary seismic network, called NAMASTE [Karplus et al., 2015; Pant et al., 2016; Mendoza et al., 2016; Ghosh et al., 2017; Karplus et al., 2017; Bai et al., 2019; Mendoza et al., 2019]. 47 near-source stations were deployed; in comparison, the permanent seismic network has only seven stations in the same area. This dataset enables us to resolve and locate aftershocks down to magnitude 2.0. Based on this well-resolved aftershock catalog, we will discuss the relationship between the aftershocks and the 3D fault structure in central Nepal.

Data

About 50 days after the Gorkha earthquake a temporary seismic network called NAMASTE was deployed in the epicentral area of the mainshock to record the aftershocks [Karplus et al., 2015; Pant et al., 2016; Mendoza et al., 2016; Ghosh et al., 2017; Karplus et al., 2017; Bai et al., 2019; Mendoza et al., 2019]. This network included broadband seismometers, short-period seismometers, and accelerometers. For our research, we used 42 broadband and short-period records covering the period from June 25, 2015, to May 14, 2016. The average spacing of the stations was

[1]Disaster Prevention Research Institute, Kyoto University, Uji, Gokasho, 611-0011, Japan
[2]Department of Mines and Geology, Kapurdhara Marg-9, Lainchour, Kathmandu, Nepal
[3]Meteorological Research Institute, 1-1 Nagamine, Tsukuba, Ibaraki 305-0052, Japan
[4]University of California, Riverside, Riverside, CA, 92521, US

0886-6236/20/$12.00

about 20 km. The three component continuous waveforms were downloaded from the IRIS Data Management Center website.

Methods

Phase Detection by the T^{pd} Method

Seismic waveforms were processed by first correcting the instrumental response and removing the DC offset. Then, we applied a fourth-order one-pass band-pass filter with a corner frequency of 2–10 Hz. Phase arrivals were detected using the T^{pd} method [Hildyard et al., 2008; Hildyard and Rietbrock, 2010]. This method identified seismic phase arrivals by observing the change in frequency of the waveforms. After applying the T^{pd} method, the arrival time was refined by following the methods of Yamada [2017]. Figure S1 shows an example of the automatic phase detection.

Once a phase arrival was detected, the refined arrival time and the maximum vertical velocity 5 s after the P-wave onset were computed. They were used for the hypocenter determination. The ratio between the maximum horizontal amplitude and the maximum vertical amplitude (H/V) in 1 s was used to classify P- and S-waves. If H/V < 0.5 or H/V > 2, the phase was classified as a P-wave or S-wave, respectively. Otherwise, the phase was treated as an indeterminate type of wave, and the automatic determination algorithm (explained in the next subsection) identified the phase that best fits the travel-time curve. Note that this picking program was tuned to detect P-wave arrival, so there were more P-wave observations than S-wave observations.

Automatic Hypocenter Determination

We implemented an automatic hypocenter determination method using Bayesian estimation [Tamaribuchi, 2018] to create an earthquake catalog. The program read a set of arrival times and maximum vertical amplitudes and created a subset of observations that were matched to a possible earthquake location. The closest 10 stations from the first trigger station were defined as a trigger group. Once three or more stations in the group were triggered within the theoretical travel-time limit, the hypocenter calculation began.

In order to determine the location, virtual hypocenters (i.e., particles) were distributed in 3D space. The weight of each particle (i.e., the likelihood that the particle represents the actual hypocenter) was computed by taking the inverse of the difference between the observed and the theoretical values. We assumed that this error followed the normal distribution. Therefore, if the location was correct, the error between the observation and the theoretical value would be small and the weight would be large.

We then used an importance sampling algorithm to refine the hypocenter location [Wu et al., 2014]. A resampling process was performed so that the particle distribution reflected the probability density function of the hypocenter location. When the likelihood calculation and resampling were repeated, virtual hypocenters gradually converged on the true hypocenter. The program stopped the iteration process when the virtual hypocenter with the maximum weight did not change after three successive iterations. It produced a final hypocenter location only if all the following conditions were satisfied: 1) the longitude and latitude errors were both less than 10 min (about 18 km), 2) the origin time error was less than 2.0 s, 3) the depth error was less than 100 km, and 4) 5 or more phases were used for the location determination.

After determining the hypocenters, we calculated the magnitude using the Nepalese attenuation model that was proposed by Baillard et al. [2017]. We selected the five closest stations for each event and fixed the time window from the theoretical P-wave arrival time to three times the difference between the arrivals of the theoretical S- and P-waves. We used the following equation to obtain the magnitude [Baillard et al., 2017]:

$$M = 0.9 \log 10(A) + 1.2 \log 10(R) + 0.0003R - 0.9, \quad (1)$$

where A was the maximum amplitude of the vertical displacement in that time window (nanometers) and R was the distance from hypocenter to station in kilometers. The median value of the five stations is chosen as the event magnitude.

Refinement of the Phase Detection

In order to improve the accuracy in the depth direction, we searched the P- and S-wave arrivals at around the theoretical arrival times based on the catalog we constructed. We used the phase detection method with the variance ratio [Tamaribuchi, 2018].

First, we applied a band-pass filter with a corner frequency of 5–10 Hz for the three component waveforms to reduce noise from tidal or distant events. We used waveforms for which either the P- or S-phase was detected by the T^{pd} method. The two horizontal waveforms were rotated to radial and transverse directions. We used the vertical and radial components to detect P- and S-phases respectively. Next, we computed the variance ratio r_{var} of the filtered waveforms for a few seconds before and after the theoretical arrival time. The r_{var} was defined as:

$$r_{var}(t) = \sum_{i=t}^{t+N-1} (x_i - \overline{x}(t))^2 / \sum_{i=t-N}^{t-1} (x_i - \overline{x}(t-N))^2, \quad (2)$$

where x_i was the filtered waveform data at the time step i, $\overline{x}(t)$ was the average of the data, i.e., $\sum_{i=t}^{t+N-1} x_i/N$, and N was the length of the data. We used the number of samples in one second for N. If the variance ratio exceeds 9 in the few seconds time window, we computed the time recording the peak of r_{var}, and used it as an arrival time.

Finally, we refined the P-wave arrival time by the autoregressive Akaike Information Criterion (AR-AIC) method [Takanami and Kitagawa, 1988, 1991]. In the AR-AIC method, a few second data before and after the estimated arrival time were treated as stationary noise and signal, respectively, and modeled as an AR process. The time series of the AIC value was expected to be the minimum at the phase arrival time. We applied this process only for the P-wave arrival, since the method did not work well for the S-wave.

After this phase detection process using variance ratio, the number of the S-wave picking increased from 61,266 to 87,621, and that of the P-wave slightly changed from 133,088 to 138,436.

Joint Hypocenter Determination

We used the VELEST program to perform the joint hypocenter determination (JHD) [Kissling et al., 1994, 1995]. VELEST was a FORTRAN77 routine that simultaneously determines the location of a group of events, the 1D velocity model, and station corrections that account for lateral velocity variations.

First, we selected relatively well-located earthquakes from our catalog. The selected events were the earthquakes where the number of picks is $\geq$20 and the azimuthal gap of the stations is $\leq$240 (see Result Section on these criteria). We defined these 3,304 events as well-located earthquakes. The waveform alignment of these events were visually inspected and we confirmed that they were all real earthquakes.

The initial velocity model was, as described by Pandey et al. [1995], a three-layer model with boundaries at 23 and 55 km depths. We subdivided this model into layers with a 2 km interval for 0–10 km, and a 5 km interval for 10–60 km. We chose station NA280 as the reference station (i.e., no station correction) since it was near the center of the aftershock distribution.

After performing the joint hypocenter determination, the program was run in single event mode to relocate all earthquakes with a fixed velocity model and station corrections. In total, 14,721 events were detected for the 11 month period.

Results

Spatiotemporal Distribution of Aftershocks

Figure 2 shows the temporal and spatial distribution of aftershocks. Large clusters are present along the northern side of the Gorkha–Pokhara anticlinorium (GPA), divided by the seismic gap north of Kathmandu. The eastern cluster is very dense and spans about 100 km parallel to the MBT fault line. The western cluster is sparse and scatters in the EW direction. Smaller clusters exist about 20 km west of Kathmandu and about 40 km east–southeast of Kathmandu. These clusters are much shallower than the large clusters.

Figure 2a shows the temporal variation of the aftershock sequence. Since our catalog data starts after June 25, 2015, we used a catalog created by Baillard et al. [2017] for earlier dates. Only well-located events (with epicentral errors of <7 km and depth errors of <10 km) in the Baillard et al. [2017] are used. Compared with the previous study, our catalog has more earthquakes and shallower events. The seismicity west of Kathmandu decays faster whereas the eastern seismicity around the largest aftershock is still active after 1 year.

In order to investigate the depth variation, the NS and EW cross sections are shown in Figure 3. Aftershocks within ± 5 km from each section line are shown in the figure. The cross sections show that the aftershocks are distributed in the shallow area, between 0 and 20 km. In the NS section (Sections A1 and A2), the depth of the aftershocks becomes deeper from the south to the north, which is consistent with the dip direction of the MHT. For example, there are two clusters in Section A2: the southern cluster is about 5 km shallower than the northern cluster. Another feature is that most of the aftershocks are distributed in the hanging wall between the ground surface and MHT fault boundary. The depth variation in the EW section (Sections B1) is not as obvious as the NS section. It seems the depth is about constant in this direction. There is a gap with few events between 80 and 100 km from the west end.

We plot the histograms of the magnitude of the catalog in Figure 4a. The magnitude distribution follows the Gutenberg-Richter law, and the minimum magnitude of complete recording (magnitude of completeness) is estimated about M2 from Figure 4a, which is smaller than in previous studies (M4.0 for Adhikari et al. [2015] and M2.5 for Baillard et al. [2017]).

Estimated 1D Velocity Model

VELEST program simultaneously determines the location of earthquakes, the 1D velocity model, and station corrections. Figure 5 and Table 1 show the optimal velocity model and station corrections. Additionally, we have performed this joint hypocenter determination with a different initial model (JMA2001, Ueno et al. [2002]), but the results are similar. The P-wave velocity (Vp) at depths <20 km is almost constant, and estimated to be 6.0 km/s. This is slightly larger than Vp obtained in a previous study; 5.6 km/s in Pandey et al. [1995], 5.7 km/s in Monsalve et al. [2006] for eastern Nepal, and 5.8 km/s in Negi et al. [2017] for west of Nepal. This value is similar to Vp of the shallow continental crust [Christensen and Mooney, 1995]. From 20 km depth, Vp gradually increased as the depth increased, to 60 km depth, and we did not observe any strong velocity contrasts. However, we may not have enough resolution at depths >20 km because of the limited number of deep earthquakes in our dataset.

Station corrections have spatial variations, and values are larger in the south (see Figure 5b). This southern part of Nepal is a lowland area formed by Himalayan rivers, called Terai. The surface structure consists of alluvial deposits, so we would expect to see a slower Vp at shallow depth. Larger values for station corrections are likely to reflect this low-velocity structure. Note that the numbers of P-wave observations at stations NA080, NA090, NA330, and NA400 are smaller (less than 100 picks), so they may have poor resolution and show a different pattern from the surrounding stations.

Uncertainty of the Phase Detection

We have evaluated the error of the automatic phase detection method by using the waveforms of the 31 well-located earthquakes on July 1, 2015. Figure S2 shows the waveforms for radial and vertical components as a function of the epicenter distance. They show a good alignment for both P- and S-phases, so these events are not noises, and the locations are mostly correct.

We manually pick the P-wave arrival of the 584 waveforms and the S-wave arrival of the 337 waveforms. The histogram of the residuals between the manual and automatic detections is shown in the Figures 6a and 6b. The rms (root mean square) error of the P-phases is 0.14 s. The waveforms at the distant stations have multiple phases at around the S-wave arrival, so it is difficult to detect the correct S-wave arrival time. Therefore, average rms error of the S-phases is as large as 0.77 s. If we remove the stations at the epicenter distance larger than 80 km, the rms error decreases to 0.35 s. The error of the automatic method is considered acceptable compared to the uncertainty of the velocity structure and local site conditions, which is on the order of a second.

Figure 6c shows the error between the observed and estimated arrival times after the relocation, as a function of the epicenter distance. The rms error for the P-phase is 0.38 s, and that for the S-phase is 1.03 s. The P-phase error is about constant for any distance, but S-phase error increases as a function of the distance. As shown in Figure S2, the S-wave arrivals at the distant station have an emergent onset, which makes it difficult to detect S-phases accurately. Note that the phase arrival times at the stations close to the epicenter are more sensitive to the depth of the event. For this dataset, the rms error of the S-phase at the stations within 30 km from the epicenter is only 0.45. Therefore, we think our phase detection has reasonable accuracy.

Uncertainty of the Aftershock Catalog

Figure 7 shows histograms of the rms, the hypocenter location error in the X (longitude), Y (latitude), and Z (depth) directions before the relocation by VELEST. The average rms is 0.66 s, and the depth error is larger than the horizontal error. The error in the X direction is slightly smaller than that in the Y direction, due to the network geometry. In order to evaluate the effect of the number of phase detections, we plot the relationship between the number of phase detections and the above uncertainty parameters in Figure 8. The rms residuals increase as a function of the number of phase detections, whereas the uncertainty of the location decreases as the number of phase detections increases. As the number of phase detections increases, in general, the distance from the hypocenter to the station increases. The uncertainty of the velocity structure accumulates for distant stations, which results in the larger rms.

If we select earthquakes determined by 20 picks or more, we are able to filter out most of the earthquakes with horizontal errors larger than 3.5 km. In order to remove earthquakes far from the network, we used earthquakes with an azimuthal gap of stations less than 240 degree. By applying this condition on the network geometry, we are able to filter out the earthquakes with relatively large errors in

Figure 8 (gray circles above the line of y=20). Therefore, we define these earthquakes, i.e. earthquakes with 20 or more phase detections and azimuthal gap of the stations less than 240 degree, as well-located earthquakes. Figures 2 and 3 show the well-located earthquakes with larger symbols. They largely represent the distribution of the whole aftershock catalog.

The seismic network that we use in this study covers the fault rupture area with about 20 km spacing. With this station spacing, it may be difficult to resolve the shallow depth earthquakes. Waveforms with both P-wave and S-wave phase detections contribute for a good depth control. In our dataset, about 60% of the phase detected waveforms have both P-wave and S-wave observations. Figure S3 shows the theoretical arrival times for different source depth. The arrival times at the closer distance shows a larger difference, and the apparent velocity is faster for the deeper earthquake. Suppose we have a station at the epicenter distance 10 km, the difference of the S-P arrival time for the depth 5 km and 15 km is 0.8 s. We think this difference can be resolved, even if we have an uncertainty in the automatic phase detection.

Change of Earthquake Distribution by the Relocation

We have performed a two-step hypocenter relocation using the VELEST program. Figure 9 shows the histograms of the rms error before and after the relocation. By adding the station correction factor and optimizing the 1D velocity structure, the average rms error of the well-located earthquakes decreased from 0.66 to 0.46 s. The average rms error of the whole catalog also was reduced from 0.44 to 0.31 s.

Figure 10 shows the earthquake locations before and after the relocation. The horizontal differences are very small inside the seismic network, whereas the earthquakes outside of the network move away from the network by a few tens of km after the relocation. This is because the inverted velocity model was faster than the initial model.

Figure 11 shows the depth of the earthquakes before and after the relocation. In order to clarify the effect of the velocity structure and station correction, the catalog with the initial velocity model and station correction, and the catalog with the optimal velocity model and no station correction, are also shown in the Figure.

The optimal velocity structure is faster than the initial velocity structure. Therefore, to make the apparent velocity slower (i.e., make the theoretical arrival times later), the depths of the earthquakes tend to be shallow (see Figures 11a and 11c).

The station corrections are positive at the stations in Terai, where the epicenter distance is large in general. Therefore, if we consider the station correction, the theoretical arrival times at the distant station become later, and the apparent velocity becomes slower. This is similar to change the velocity model slower. Therefore, the depth of the earthquakes becomes deeper (see Figures 11a and 11b).

If we consider both the optimal velocity model and station correction, the depth of the well-located earthquakes does not change so much (see Figures 11a and 11d). However, the distribution of other earthquakes, shown as gray circles in Figure 11, is scattered in the shallow depth before the relocation, and became more confined after.

Discussion

Comparison with the previous catalog

There is a similar pattern for the distribution of aftershocks in the previous aftershock studies [e.g. Adhikari et al., 2015; Baillard et al., 2017], but our study has greater spatial resolution due to the data from the dense seismic network made available to us. Our catalog has smaller magnitude of completeness than that in the previous study and more aftershocks than those of the same period [e.g. Baillard et al., 2017], as shown in Figure 2a. Our catalog and Baillard et al. [2017] have an overlapped period for about one month. Figure S4 shows the 669 earthquakes with the difference of the origin time less than 3 s and the difference of the horizontal location less than 20 km. The horizontal differences are very small inside the seismic network, and larger at the border between China and Nepal. In the section profile, our catalog shows more tightly clustered depth estimates than Baillard et al. [2017]. The depth change in the dip direction of the MHT was not clearly observed in the previous study.

The spatial resolution was improved owing to the joint hypocenter determination. The average rms error decreased from 0.66 s to 0.46 s, and the estimated station corrections were consistent with the subsurface geological structure. Although our catalog lacks the first two months of aftershocks, it is a well-resolved catalog resulting from the many near-source seismic stations in the fault rupture area.

Aftershocks and 3D structure model

In order to examine the relationship between the aftershocks and the 3D fault structure, a 3D MHT structure model [Hubbard et al., 2016] has been included in Figures 2b and 3. This model was developed from the geological cross section of central Nepal and extended laterally using the MFT, MBT, and GPA surface traces as a proxy [Hubbard et al., 2016]. There are two ramp structures parallel to the MBT and GPA near Kathmandu, and the middle décollement is also bounded by two ramps.

Comparison of the cross sections and the aftershock data shows that most aftershocks are confined between the ground surface and the MHT shear zone. The aftershock depths not only match the slip surface, but are also scattered throughout the entire hanging wall. The bottom of the aftershock distribution is consistent with the MHT model.

Figure 12 shows the aftershock distribution and mainshock source model [Kobayashi et al., 2016]. According to Hubbard et al. [2016], the location of the large slip is consistent with the location of the middle décollement between the two ramp structures. Our aftershock distribution image shows that there are fewer events in the large slip area and more events on the two ramp structures surrounding the large slip area. This is consistent with the observation of other large earthquakes [e.g. Das and Henry, 2003; Shearer et al., 2003; Yukutake and Iio, 2017]. The western aftershocks were much more densely distributed than the eastern aftershocks, and the very dense area seems to be parallel to the GPA. Interestingly, the large clusters of earthquakes at the northern side of the GPA is located above the deeper ramp in the model, and the small cluster south of the GPA is located above the shallower ramp.

Comparison with the previous seismicity before the Gorkha earthquake shows that the large clusters at the northern side of the GPA exist before the Gorkha earthquake [Ader et al., 2012; Stevens and Avouac, 2015]. The locations are consistent with areas with a large gradient of coupling (the downdip edge of the locked MHT fault zone) where stress buildup is at a maximum [Stevens and Avouac, 2015; Avouac et al., 2015]. There is almost no seismicity south of the GPA prior to the Gorkha earthquake [Ader et al., 2012; Stevens and Avouac, 2015]. The Gorkha earthquake ruptured the lower edge (northern end) of the locked MHT, which, we assume, has activated the southern clusters. We propose that these smaller clusters south of the GPA are generated by the stress heterogeneities resulting from the shallower ramp structure.

Conclusions

In this paper, we created a well-resolved aftershock catalog covering the time period up to 11 months after the 2015 Gorkha earthquake by processing data from the NAMASTE temporary seismic network that was deployed in a near-source region. We identified about 15000 events, with the magnitude of completeness of M2.

Our catalog shows two major clusters north of the GPA and smaller clusters in the south. The southern clusters are shallower than those of the northern clusters, which is consistent with the dip direction of the MHT. Most aftershocks are confined between the ground surface and the MHT shear zone, and their distribution may reflect structural complexity along the MHT.

Our aftershock distribution shows that there are fewer events in the large slip area, and the clusters occurred on the two ramp structures in the 3D MHT model surrounding the large slip area. This may suggest a larger stress accumulation on the ramp structures. Compared with the previous seismicity before the Gorkha earthquake, there is almost no seismicity south of GPA. The Gorkha earthquake ruptures the lower edge of the locked MHT, which may have activated the southern clusters.

We obtain a 1D velocity structure and station correction factors using a joint hypocenter determination. The P-wave velocity at depths of <20 km was almost constant at 6.0 km/s, which is similar to Vp of the shallow continental crust.

Data and Resources

We use the seismic waveform data obtained by the group of the Department of Mining and Geology in Nepal, the University of California at Riverside, the University of Texas at El Paso, Stanford University, and Oregon State University. The seismic data is available on the IRIS Data Management Center website at `https://www.fdsn.org/networks/detail/XQ_2015/`. (last accessed July 2019). Some plots were made using the Generic Mapping Tools version 4.5.7 [Wessel and Smith, 1991]. The supplemental material contains four figures (Figures S1 to S4) and the aftershock catalog (Table S1).

Acknowledgments. We thank the entire NAMASTE team including students, staffs, and scientists from the Department of Mining and Geology in Nepal, the University of California at Riverside, the University of Texas at El Paso, Stanford University, and Oregon State University for operating the temporary seismic network in Nepal. We appreciate valuable comments from Dr. Jim Mori in Kyoto University.

References

Ader, T., Avouac, J., Liu-Zeng, J., Lyon-Caen, H., Bollinger, L., Galetzka, J., Genrich, J., Thomas, M., Chanard, K., and Sapkota, S. N. (2012). Convergence rate across the Nepal Himalaya and interseismic coupling on the Main Himalayan Thrust: Implications for seismic hazard. *Journal of Geophysical Research: Solid Earth*, 117(B4).

Adhikari, L., Gautam, U., Koirala, B., Bhattarai, M., Kandel, T., Gupta, R., Timsina, C., Maharjan, N., Maharjan, K., and Dahal, T. (2015). The aftershock sequence of the 2015 April 25 Gorkha-Nepal earthquake. *Geophysical Journal International*, 203(3):2119–2124.

Avouac, J.-P., Meng, L., Wei, S., Wang, T., and Ampuero, J.-P. (2015). Lower edge of locked Main Himalayan Thrust unzipped by the 2015 Gorkha earthquake. *Nature Geoscience*, 8(9):708.

Bai, L., Liu, H., Ritsema, J., Mori, J., Zhang, T., Ishikawa, Y., and Li, G. (2016). Faulting structure above the Main Himalayan Thrust as shown by relocated aftershocks of the 2015 Mw7.8 Gorkha, Nepal, earthquake. *Geophysical Research Letters*, 43(2):637–642.

Bai, L., Klemperer, S., Mori, J., Karplus, M., Ding, L., Liu, H., Li, G., Song, B., and Dhakal, S. Lateral variation of the Main Himalayan Thrust controls the rupture length of the 2015 Gorkha earthquake in Nepal. *Science Advances*, 5(6):eaav0723.

Baillard, C., Lyon-Caen, H., Bollinger, L., Rietbrock, A., Letort, J., and Adhikari, L. B. (2017). Automatic analysis of the Gorkha earthquake aftershock sequence: evidences of structurally segmented seismicity. *Geophysical Journal International*, 209(2):1111–1125.

Christensen, N. I. and Mooney, W. D. (1995). Seismic velocity structure and composition of the continental crust: A global view. *Journal of Geophysical Research: Solid Earth*, 100(B6):9761–9788.

Dahal, R. (2006). Geology for technical students. *Bhrikuti Academic Publication, Kathmandu*, 756.

Das, S. and Henry, C. (2003). Spatial relation between main earthquake slip and its aftershock distribution. *Reviews of geophysics*, 41(3).

Galetzka, J., Melgar, D., Genrich, J. F., Geng, J., Owen, S., Lindsey, E. O., Xu, X., Bock, Y., Avouac, J.-P., and Adhikari, L. B. (2015). Slip pulse and resonance of the Kathmandu basin during the 2015 Gorkha earthquake, Nepal. *Science*, 349(6252):1091–1095.

Ghosh, A., Mendoza, M., LI, B., Karplus, M. S., Nabelek, J., Sapkota, S. N., Adhikari, L. B., Klemperer, S. L., and Velasco, A. A. (2017). Fault structure in the Nepal Himalaya as illuminated by aftershocks of the 2015 Mw 7.8 Gorkha earthquake recorded by the local Namaste network. *AGU Fall Meeting Abstracts*.

Hildyard, M. W., Nippress, S. E., and Rietbrock, A. (2008). Event detection and phase picking using a time-domain estimate of predominate period T^{pd}. *Bulletin of the Seismological Society of America*, 98(6):3025–3032.

Hildyard, M. W. and Rietbrock, A. (2010). T^{pd}, a damped predominant period function with improvements for magnitude estimation. *Bulletin of the Seismological Society of America*, 100(2):684–698.

Hubbard, J., Almeida, R., Foster, A., Sapkota, S. N., Bürgi, P., and Tapponnier, P. (2016). Structural segmentation controlled the 2015 Mw 7.8 Gorkha earthquake rupture in Nepal. *Geology*, 44(8):639–642.

Karplus, M., Sapkota, S., Nabelek, J., Pant, M., Velasco, A., Patlan, E., Klemperer, S., Braunmiller, J., Ghosh, A., and Sapkota, B. (2015). Aftershocks of the M7.8 Gorkha (Nepal) Earthquake: Early Results from Project NAMASTE. *AGU Fall Meeting Abstracts*.

Karplus, M. S., Pant, M., Velasco, A. A., Nabelek, J., Kuna, V. M., Sapkota, S. N., Ghosh, A., Mendoza, M., Adhikari, L. B., and Klemperer, S. L. (2017). Structure and tectonics of the Main Himalayan Thrust and associated faults from recent earthquake and seismic imaging studies using the NAMASTE array. *AGU Fall Meeting Abstracts*.

Kissling, E., Ellsworth, W., Eberhart-Phillips, D., and Kradolfer, U. (1994). Initial reference models in local earthquake tomography. *Journal of Geophysical Research: Solid Earth*, 99(B10):19635–19646.

Kissling, E., Kradolfer, U., and Maurer, H. (1995). Program VELEST user's guide - short introduction. *Institute of Geophysics, ETH Zurich*.

Kobayashi, H., Koketsu, K., Miyake, H., Takai, N., Shigefuji, M., Bhattarai, M., and Sapkota, S. N. (2016). Joint inversion of teleseismic, geodetic, and near-field waveform datasets for rupture process of the 2015 Gorkha, Nepal, earthquake. *Earth, Planets and Space*, 68(1):66.

Letort, J., Bollinger, L., Lyon-Caen, H., Guilhem, A., Cano, Y., Baillard, C., and Adhikari, L. B. (2016). Teleseismic depth estimation of the 2015 Gorkha-Nepal aftershocks. *Geophysical Journal International*, 207(3):1584–1595.

McNamara, D. E., Yeck, W., Barnhart, W. D., Schulte-Pelkum, V., Bergman, E., Adhikari, L., Dixit, A., Hough, S., Benz, H. M., and Earle, P. (2017). Source modeling of the 2015 Mw 7.8 Nepal (Gorkha) earthquake sequence: Implications for geodynamics and earthquake hazards. *Tectonophysics*, 714:21–30.

Mendoza, M., Ghosh, A., Karplus, M., Nabelek, J., Sapkota, S., Adhikari, L., Klemperer, S., and Velasco, A. (2016). Along-strike variations in the Himalayas illuminated by the aftershock sequence of the 2015 Mw 7.8 Gorkha earthquake using the Namaste local seismic network. *AGU Fall Meeting Abstracts*.

Mendoza, M., Ghosh, A., Karplus, M., Klemperer, S., Sapkota, S., Adhikari, L., and Velasco, A. (2016). Duplex in the Main Himalayan Thrust illuminated by aftershocks of the 2015 Mw 7.8 Gorkha earthquake. *Nature Geoscience*, doi:10.1038/s41561-019-0474-8 (in press).

Monsalve, G., Sheehan, A., Schulte-Pelkum, V., Rajaure, S., Pandey, M., and Wu, F. (2006). Seismicity and one-dimensional velocity structure of the Himalayan collision zone: Earthquakes in the crust and upper mantle. *Journal of Geophysical Research: Solid Earth*, 111(B10).

Nábělek, J., Hetényi, G., Vergne, J., Sapkota, S., Kafle, B., Jiang, M., Su, H., Chen, J., and Huang, B.-S. (2009). Underplating in the Himalaya-Tibet collision zone revealed by the Hi-CLIMB experiment. *Science*, 325(5946):1371–1374.

Negi, S. S., Paul, A., Cesca, S., Kriegerowski, M., Mahesh, P., and Gupta, S. (2017). Crustal velocity structure and earthquake processes of Garhwal-Kumaun Himalaya: Constraints from regional waveform inversion and array beam modeling. *Tectonophysics*, 712:45–63.

Pandey, M., Tandukar, R., Avouac, J., Lave, J., and Massot, J. (1995). Interseismic strain accumulation on the Himalayan crustal ramp (Nepal). *Geophysical Research Letters*, 22(7):751–754.

Pandey, M., Tandukar, R., Avouac, J., Vergne, J., and Heritier, T. (1999). Seismotectonics of the Nepal Himalaya from a local seismic network. *Journal of Asian Earth Sciences*, 17(5-6):703–712.

Pant, M., Velasco, A., Karplus, M., Patlan, E., Ghosh, A., Nabelek, J., Kuna, V., Sapkota, S., Adhikari, L., and Klemperer, S. (2016). Aftershock stress analysis of the April 2015 Mw 7.8 Gorkha earthquake from the NAMASTE project. *AGU Fall Meeting Abstracts*.

Shearer, P. M., Hardebeck, J. L., Astiz, L., and Richards-Dinger, K. B. (2003). Analysis of similar event clusters in aftershocks of the 1994 Northridge, California, earthquake. *Journal of Geophysical Research: Solid Earth*, 108(B1).

Stevens, V. and Avouac, J. (2015). Interseismic coupling on the Main Himalayan Thrust. *Geophysical Research Letters*, 42(14):5828–5837.

Takanami, T. and Kitagawa, G. (1988). A new efficient procedure for the estimation of onset times of seismic waves. *Journal of Physics of the Earth*, 36(6):267–290.

Takanami, T. and Kitagawa, G. (1991). Estimation of the arrival times of seismic waves by multivariate time series model. *Annals of the Institute of Statistical mathematics*, 43(3):407–433.

Tamaribuchi, K. (2018). Evaluation of automatic hypocenter determination in the JMA unified catalog. *Earth, Planets and Space*, 70:141.

Tilmann, F., Ni, J., and INDEPTH III, S. T. (2003). Seismic imaging of the downwelling Indian lithosphere beneath central Tibet. *Science*, 300(5624):1424–1427.

Ueno, H., Hatakeyama, S., Aketagawa, T., Funasaki, J., and Hamada, N. (2002). Improvement of hypocenter determination procedures in the Japan meteorological agency. *Quarterly Journal of Seismology*, 65:123–134.

Wang, X., Wei, S., and Wu, W. (2017). Double-ramp on the Main Himalayan Thrust revealed by broadband waveform modeling of the 2015 Gorkha earthquake sequence. *Earth and Planetary Science Letters*, 473:83–93.

Wessel, P. and Smith, W. (1991). Free software helps map and display data. *Eos*, 72(441):445–446.

Wu, S., Yamada, M., Tamaribuchi, K., and Beck, J. (2014). Multi-events earthquake early warning algorithm using a Bayesian approach. *Geophysical Journal International*, 200(2):791–808.

Yamada, M. 2017). Prototype of P-wave Detection Algorithm for Earthquake Early Warning. *Seismological Society of Japan annual meeting Abstracts*.

Yukutake, Y. and Iio, Y. (2017). Why do aftershocks occur? Relationship between mainshock rupture and aftershock sequence based on highly resolved hypocenter and focal mechanism distributions. *Earth, Planets and Space*, 69(1):68.

M. Yamada, Kyoto University, Uji, Gokasho, 611-0011, Japan (masumi@eqh.dpri.kyoto-u.ac.jp)

Figures and Tables

Table 1. Initial and optimal models for the P-wave and S-wave velocity structure in km/s.

Depth (km)	Vp(ini)	Vp(opt)	Vs(ini)	Vs(opt)
0-2	5.56	6.01	3.18	3.56
2-4	5.56	6.01	3.18	3.56
4-6	5.56	6.01	3.18	3.56
6-8	5.56	6.01	3.18	3.56
8-10	5.56	6.01	3.18	3.56
10-15	5.56	6.01	3.18	3.56
15-20	5.56	6.01	3.18	3.56
20-23	5.56	6.01	3.18	3.56
23-25	6.70	6.69	3.71	3.79
25-30	6.70	6.75	3.71	3.82
30-35	6.70	6.80	3.71	3.83
35-40	6.70	6.92	3.71	3.96
40-45	6.70	6.93	3.71	4.00
45-50	6.70	7.1	3.71	4.12
50-55	6.70	7.22	3.71	4.15
55-60	8.10	8.23	4.63	4.67
60-	8.10	8.23	4.63	4.69

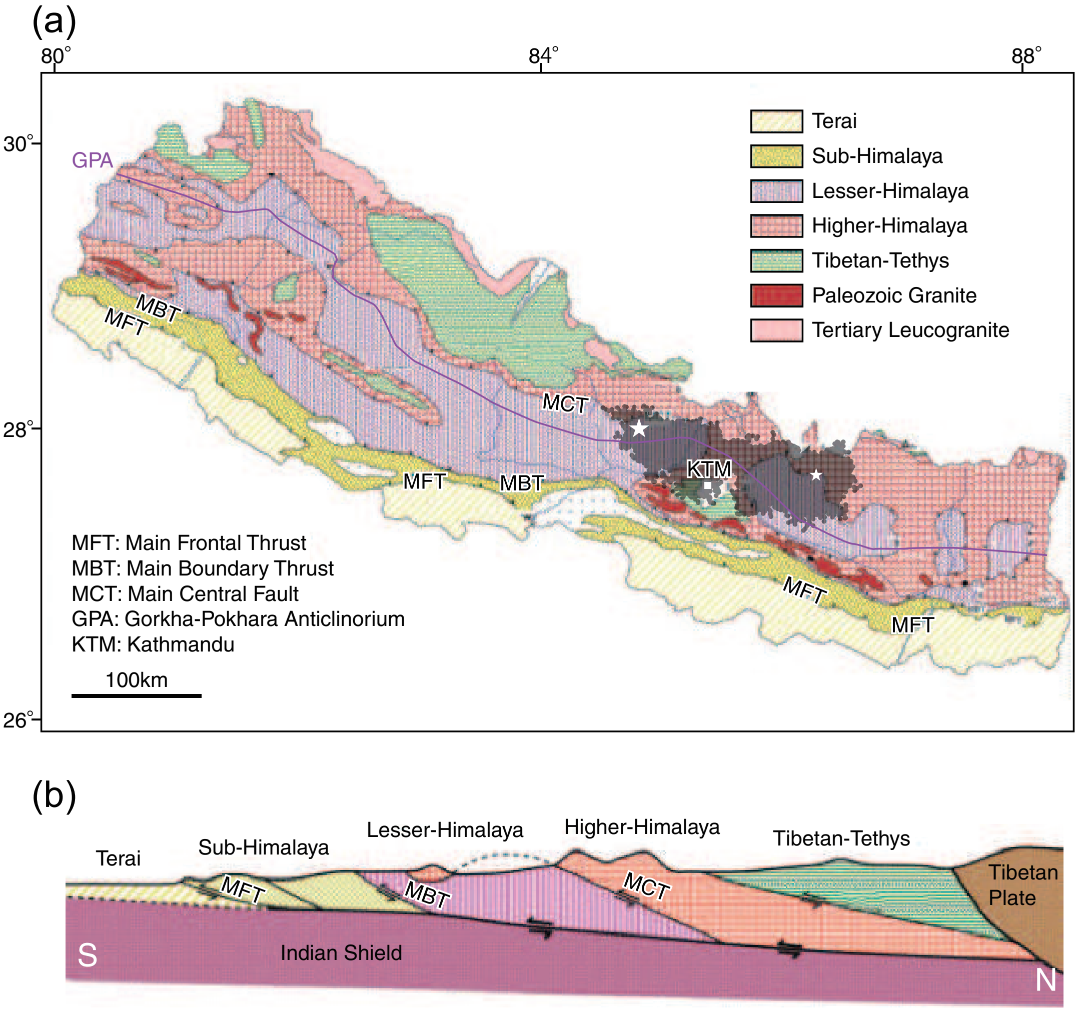

Figure 1. Geology in Nepal modified after Dahal [2006]. (a) Geological map and aftershock area shown in shaded region. Large and small stars show the location of the mainshock and the largest aftershock on May 12, respectively. (b) Schematic NS cross section.

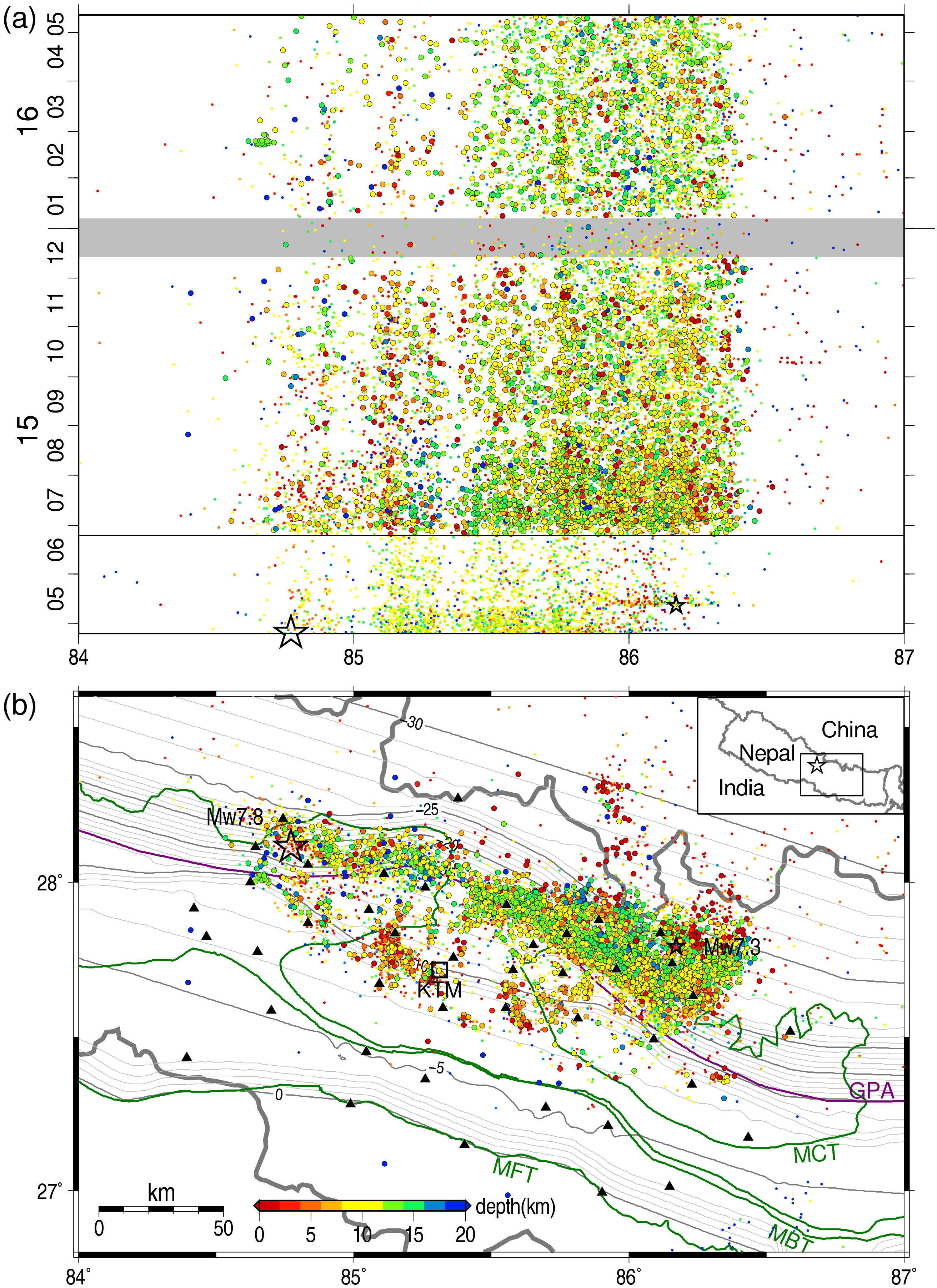
(a)
16
15
05
04
03
02
01
12
11
10
09
08
07
06
05
84
85
86
87
(b)
China
Nepal
India
Mw7.8
Mw7.3
KTM
GPA
MCT
MFT
MBT
28°
27°
km
0
50
depth(km)
0
5
10
15
20
84°
85°
86°
87°

Figure 2.

Figure 2: Spatiotemporal variation of our catalog. Larger symbol represents the well-located earthquakes. Large and small stars show the location of the mainshock and the largest aftershock on May 12, respectively. (a) Time sequence of the aftershocks. The numbers on the vertical axis represent the year (15 or 16) and the month. The shaded period lacks some data (less than 25 stations). The catalog of Baillard et al. [2017] is used before June 25, 2015. (b) Map view of the aftershock distribution. Major fault systems and the 3D MHT model are added [Hubbard et al., 2016]. The solid triangles show the locations of the temporary seismic stations. Thick gray lines show the boundary of the countries. The top right figure shows the map of Nepal and the location of the mainshock.

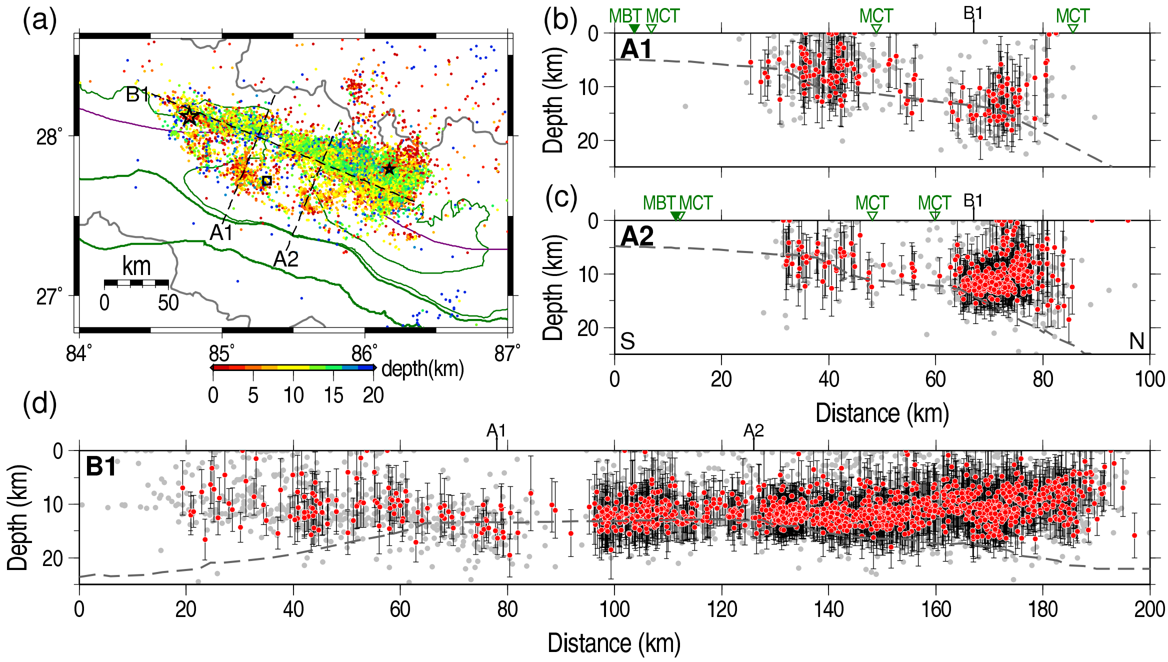

Figure 3. Profiles of the aftershocks. (a) Dashed lines show the locations of cross sections. Other symbols are in the same format as Figure 2b. (b)-(d) NS and EW sections of the aftershocks. Circles with an errorbar show the well-located earthquakes and lighter circles show all the other earthquakes. The solid and open inverted triangles show the locations of MBT and MCT, respectively. The 3D MHT model [Hubbard et al., 2016] is represented by the dashed line.

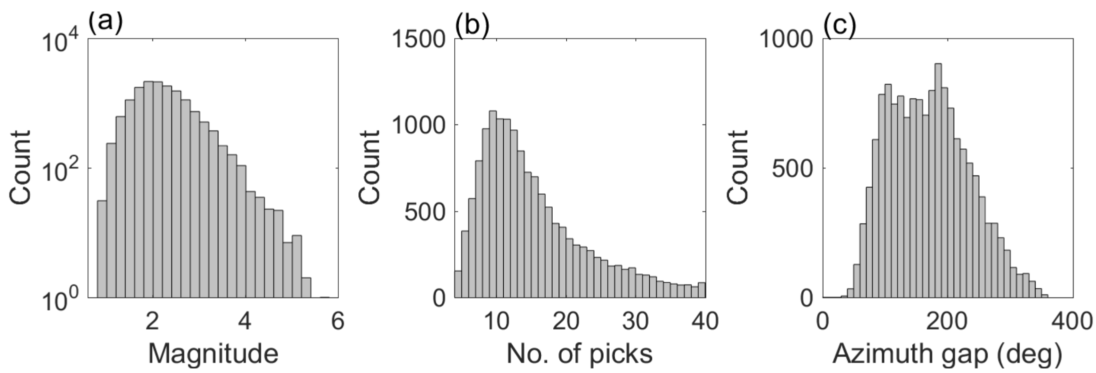

Figure 4. Histogram of the (a) magnitude, (b) number of picks used for location determination, and (c) azimuthal gap of the stations.

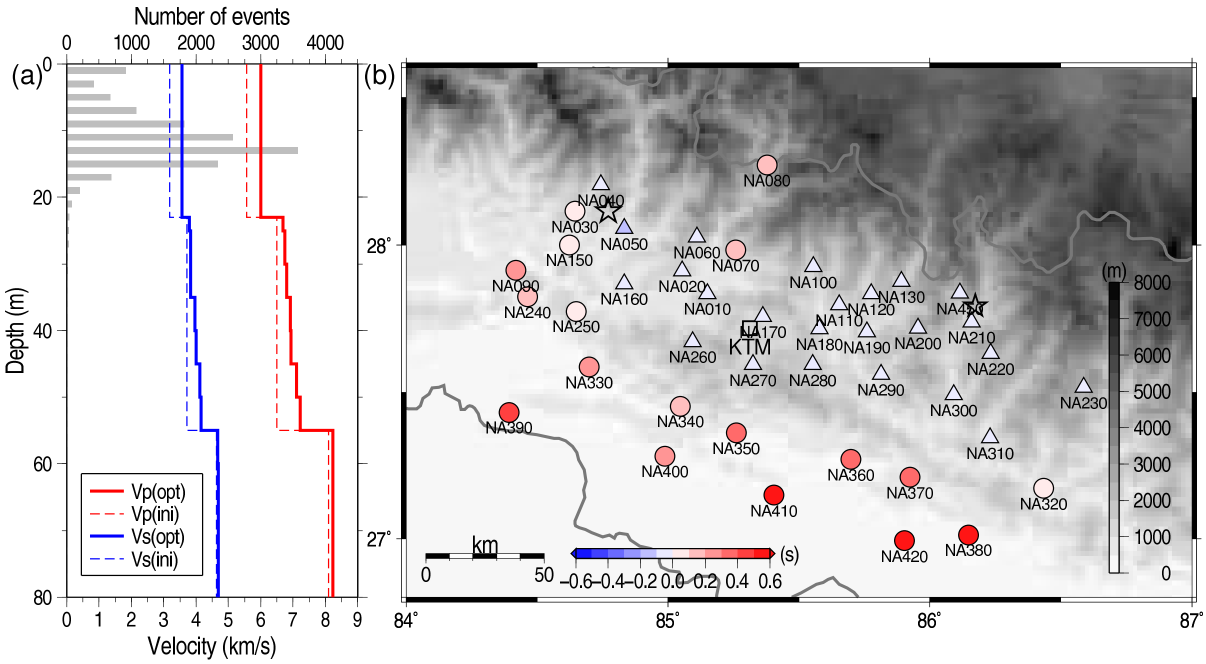

Figure 5. Results of joint hypocenter determination. (a) Initial and optimal 1D velocity models for Vp and Vs. Gray bars show the depth distribution of all earthquakes after the relocation. (b) Station correction factors at the aftershock stations. The circles and triangles show the positive and negative delay time in seconds, respectively. The background color shows the altitude. The stars mark the locations of the mainshock and the largest aftershock on May 12.

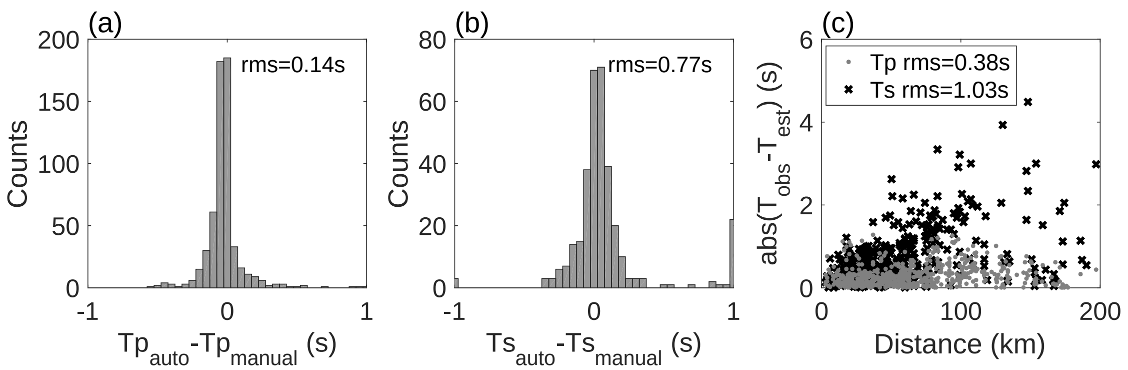

Figure 6. Histograms of the residuals for (a) automatic and manual P-wave arrival times, (b) automatic and manual S-wave arrival times, and (c) observed and estimated arrival times for P- and S-phases as a function of the epicenter distance.

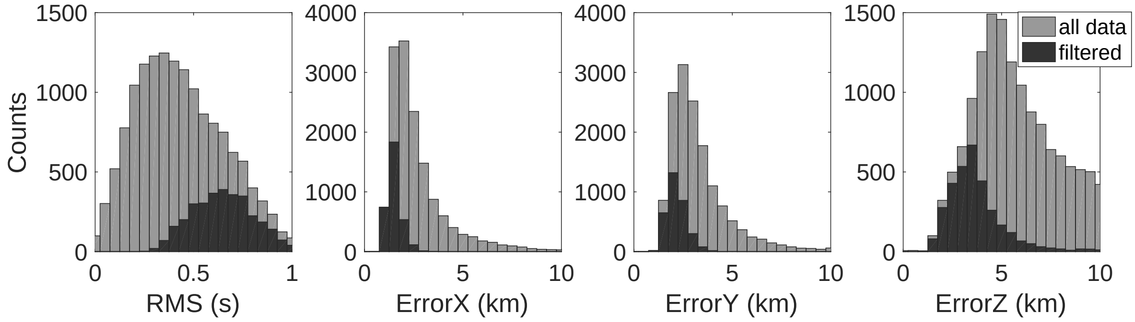

Figure 7. Histograms of the rms, the hypocenter location error in the X (longitude), Y (latitude), and Z (depth) directions before the relocation by the VELEST. Dark color shows the well-located earthquakes and gray color shows all earthquakes.

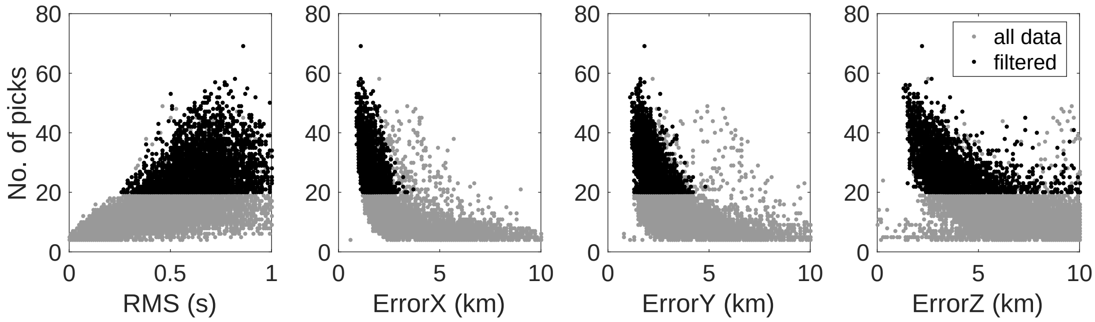

Figure 8. Relationship between the number of P- and S-phase detections vs the rms, the hypocenter location error in the X (longitude), Y (latitude), and Z (depth) directions before the relocation by the VELEST. Black circles show the well-located earthquakes and gray circles show all the other earthquakes.

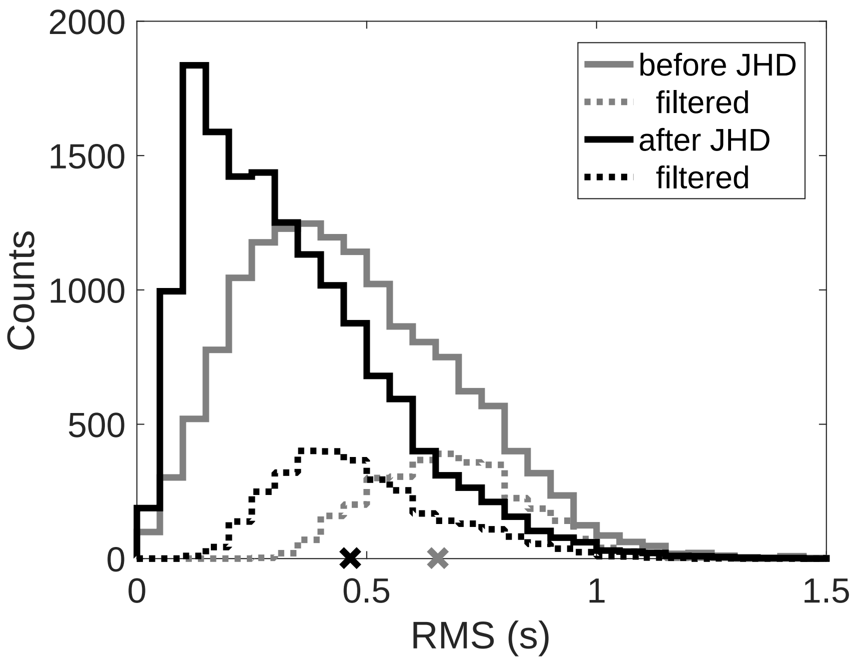

Figure 9. Histograms of the rms error before (gray) and after (black) the joint hypocenter determination. The solid and dashed lines show the histograms for the whole and well-located catalogs, respectively. Cross symbols show the average rms errors for the well-located catalog.

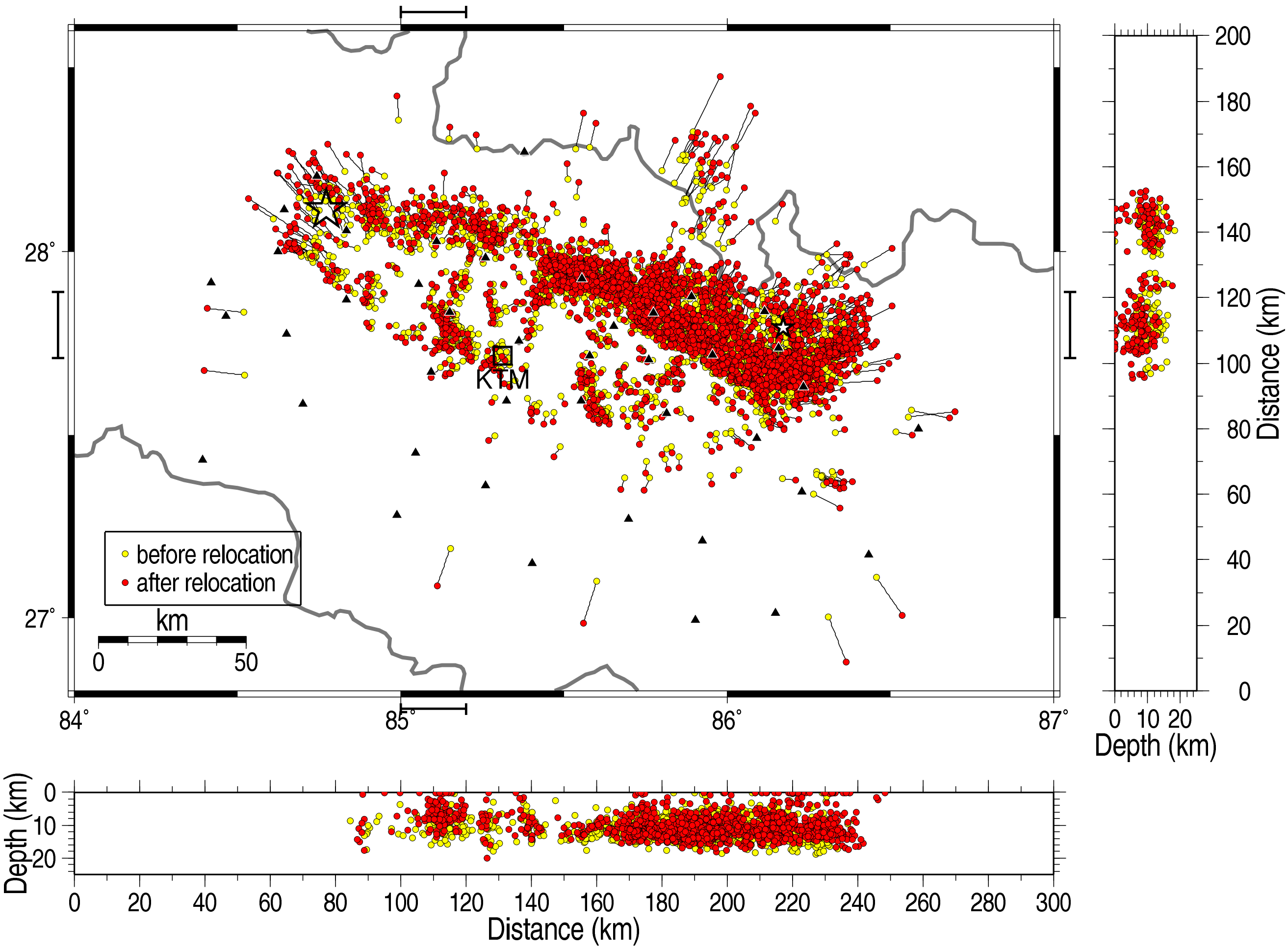

Figure 10. Comparison of the well-located earthquake locations before and after the relocation shown in small circles. The bars on the map frame show the range (20 km) of earthquakes included in the cross sections.The solid triangles show the locations of the temporary seismic stations. Large and small stars show the location of the mainshock and the largest aftershock on May 12, respectively.

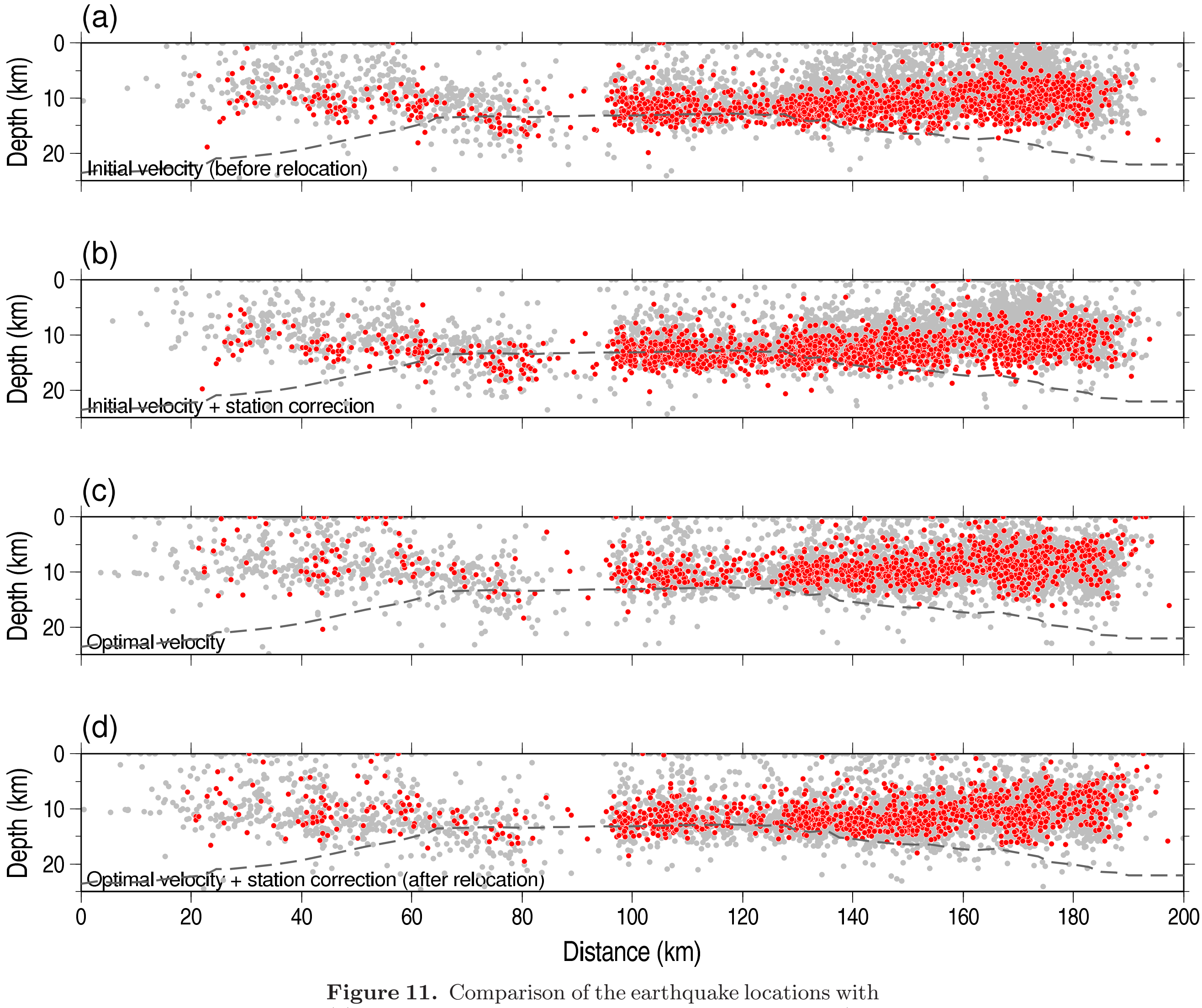

Figure 11. Comparison of the earthquake locations with (a) initial velocity model and no station correction (before the relocation) (b) initial velocity model and station correction (c) optimal velocity model and no station correction, and (d) optimal velocity model and station correction. The format is the same as the Figure 3d.

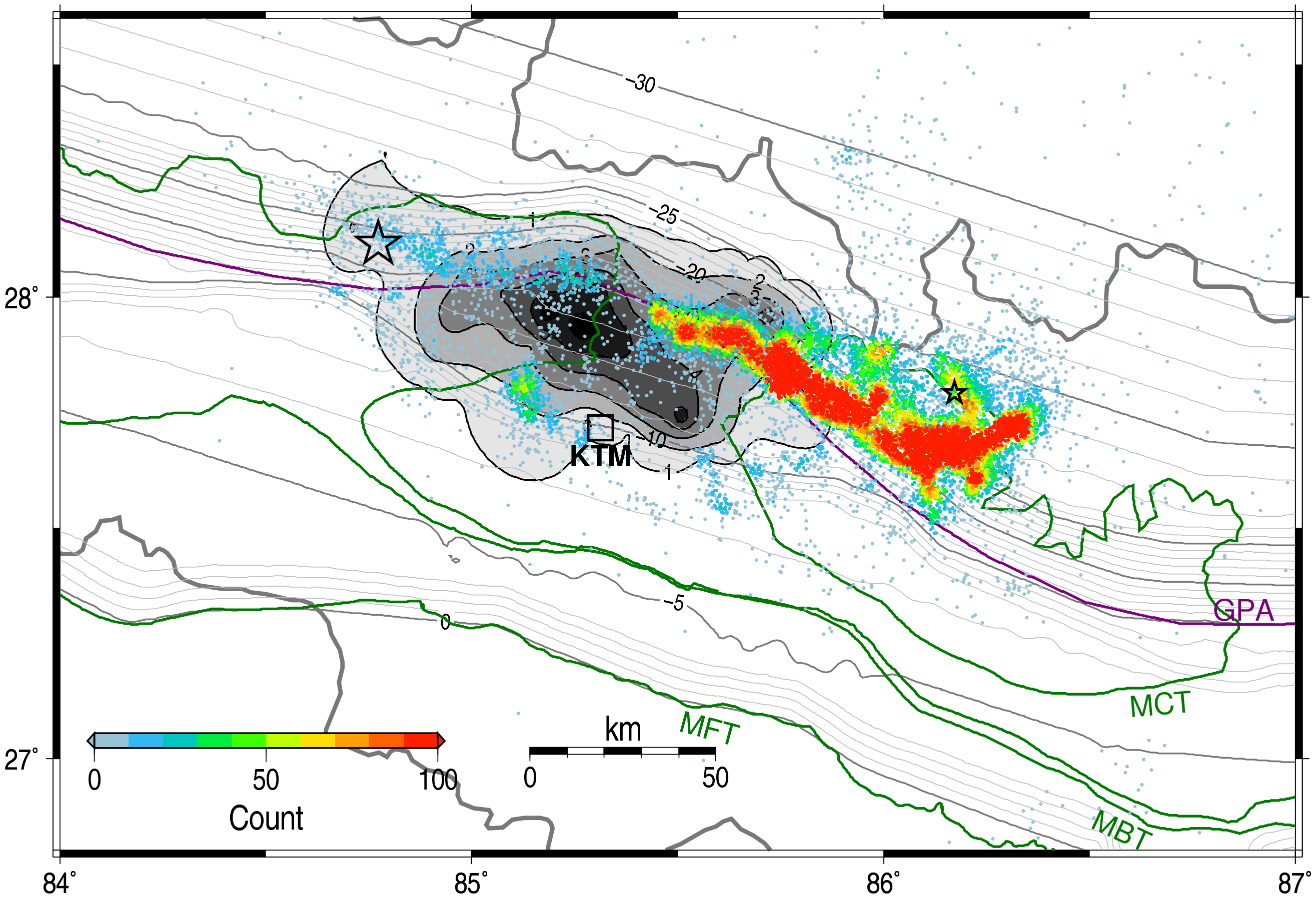

Figure 12. Aftershock locations and slip model of the mainshock [Kobayashi et al., 2016]. Gray contour shows the slip in meters, and the small circles show the frequency distribution of the aftershocks. It is the number of hypocenters within a radius of 3 km of each earthquake. Major fault systems and the 3D MHT model (in gray contours) are added. Large and small stars show the location of the mainshock and the largest aftershock on May 12, respectively.